ROYAL SOCIETY OF CHEMISTRY

PAPER

Check for updates

CaGdF$_5$ based heterogeneous core@shell upconversion nanoparticles for sensitive temperature measurement†

Xiaoyu Xie,[ab] Wang Wang,[ab] Haoran Chen,[a] Run Yang,[ab] Han Wu,[ab] Dechao Gan,[ab] Bin Li,[a] Xianggui Kong,[a] Qiqing Li[*a] and Yulei Chang [ID] [*a]

Lanthanide-doped upconversion nanoparticles (UCNPs) have attracted great attention in temperature sensing because of their widespread thermal quenching effect (TQE), a phenomenon in which luminescence intensity decreases as the temperature increases. However, enhancing the TQE of activated ions without changing the dopants or the host is still challenging. Herein, Yb^{3+} and Er^{3+} codoped UCNPs in a cubic CaGdF$_5$ host were synthesized by a coprecipitation method for optical temperature sensing. Compared with the homogeneous shell (CaGdF$_5$), those heterogeneous (CaF$_2$) shelled UCNPs exhibited stronger upconversion luminescence (UCL) due to the significantly reduced multiphonon nonradiative relaxation. Further, we investigated the effects of homogeneous and heterogeneous shells on TQE. The relationship between the intensity ratio of the green emission bands of Er^{3+} ions ($^2H_{11/2} \rightarrow {}^4I_{15/2}$ and $^4S_{3/2} \rightarrow {}^4I_{15/2}$) and temperature are obtained for these two core@shell UCNPs. The results demonstrated that the UCNPs with CaF$_2$ shells are more sensitive to temperature in the 200−300 K. The maximum thermal sensitivity of CaGdF$_5$:Yb,Er@CaF$_2$ could reach 2.2% K^{-1} at 200 K. These results indicate that the heterogeneous core@shell UCNPs are promising for use as optical temperature sensors.

1   Introduction

Optical temperature sensing based on the luminescence intensity ratio (LIR) has been used in the past decades since it allows for noninvasive thermal detection.[1–3] This sensing technique monitors temperature-dependent changes at specific thermally coupled energy levels by measuring emission intensity ratios. Lanthanide-doped UCNPs can convert long-wavelength photons to short-wavelength photons, and are considered promising probes in optical thermometry with a fast response, and great resolution and sensitivity.[4–7] It has been shown that the LIR of the thermally coupled two green bands of Er^{3+} ions varies as a function of temperature. Consequently, Er^{3+}-doped luminescent materials have been widely used as probes for thermal sensing applications.[8–13]

Besides, it is crucial to choose an appropriate host material with low crystal field symmetry[14] and low phonon energy[15] that provide an efficient luminescence signal for practical applications. On the one hand, the forbiddance of the 4f–4f electronic-dipole transitions of rare-earth ions can be broken by the crystal field symmetry of the host matrix. On the other hand, the host materials also require low phonon energy, which prevents luminescence quenching due to the nonirradiation relaxation. Lanthanide fluorides (LaF$_3$, YF$_3$ and GdF$_3$) have been taken as promising materials for upconversion luminescence because of low phonon energy. Unfortunately, these materials suffered from the high crystal field symmetry of orthorhombic phase, resulting in limited upconversion efficiencies.[16–18] Therefore, research interest turns to alkaline or alkaline-earth rare-earth fluoride (MReF) host lattices showing more efficient upconversion luminescence, such as hexagonal NaLnF$_4$, and cubic BaYF$_5$ NPs.[19–26] Recently, SrLuF host lattices have provided more efficient upconversion than β-NaGdF$_4$ with similar nanoparticle size.[27] Lanthanide-doped MReF UCNPs should be the promising host material for optical temperature sensing applications. In addition to composition optimization, the core@shell structure can also improve temperature detection sensitivity. Liu *et al.* reported core@multishell UCNPs with an enhanced thermal sensitivity three times higher than core-only NPs.[28] For preparing core@shell UCNPs, epitaxial growth is preferred for constructing the same or similar crystal structure for core and shell counterparts, such as NaYF$_4$@NaGdF$_4$. Nevertheless, the influences of shell composition on the temperature sensitivity of UCNPs have not been thoroughly investigated until now.

aState Key Laboratory of Luminescence and Applications, Changchun Institute of Optics, Fine Mechanics and Physics, Chinese Academy of Sciences, Changchun, 130033, Jilin, China. E-mail: liqiqing0742@sina.cn; yuleichang@ciomp.ac.cn

bUniversity of the Chinese Academy of Sciences, Beijing 100049, China

† Electronic supplementary information (ESI) available. See DOI: https://doi.org/10.1039/d3ra00716b

Here, we developed a thermal decomposition method to synthesize ultra-small CaGdF nanoparticles (NPs) with cubic phase. Sub-5 nm Yb^{3+} and Er^{3+} codoped CaGdF UCNPs were synthesized with an optimized Ca^{2+}/Gd^{3+} molar ratio of 1:1. Our alkaline-earth-based UCNPs doped with Yb^{3+} and Er^{3+} show mostly green and red upconversion emissions under 980 nm laser illumination. The dominant upconversion mechanism is based on Förster resonant energy transfer (FRET), which depends on the inverse distance between the dopants. What's more, we studied the influence of CaGdF and CaF_2 shells on optical properties. Due to less non-irradiation relaxation, the core@shell $CaGdF_5@CaF_2$ NPs (CGF@CF) performed higher efficient luminescence than $CaGdF_5@CaGdF_5$ NPs (CGF@CGF). Furthermore, we evaluated the thermal sensing performance of CGF@CF and CGF@CGF in the temperature range from 200 K to 300 K. The LIR of thermally coupled two green bands of Er^{3+} ions in CGF@CF is more sensitive to temperature variation, indicating the potential for these NPs as thermometers.

2 Experimental

2.1 Reagents

$Ln(CH_3COO)_3 \cdot xH_2O$ (>99%), Ln_2O_3 (Ln: Gd, Yb, Er, > 99%), $Ca(CH_3COO)_2$, CaO, NH_4F (>98%), oleic acid (OA, 90%), 1-octadecene (ODE, 90%), trifluoroacetic acid (99%), ethanol and cyclohexane were purchased from Sigma-Aldrich and used without further purification.

2.2 Synthesis of core $Ca_xGd_yF_{(2x+3y)}$:20% Yb,2% Er NPs

The synthesis of monodisperse $Ca_xGd_yF_{(2x+3y)}$:20% Yb,2% Er nanocrystals was slightly modified from the previously reported method.[27] x mmol of $Ca(CH_3COO)_2$, 0.78y mmol of $Gd(CH_3COO)_3 \cdot xH_2O$, 0.2$y$ mmol of $Yb(CH_3COO)_3 \cdot xH_2O$, and 0.02$y$ mmol of $Er(CH_3COO)_3 \cdot xH_2O$ ($x:y = 0:1, 1:1, 2:1$), 8 mL of oleic acid and 8 mL of 1-octadecene were added to a 100 mL flask under stirring. The solution was heated to 120 °C and then kept for 1 h under vacuum and then cooled to room temperature. After ($2x + 3y$) mmol of NH_4F was added, the solution was heated to 120 °C and kept for 1 h under a vacuum. Finally, the solution became a clear yellow solution. Then the solution was heated to 300 °C under a vacuum for 1 h and then cooled to room temperature. The nanocrystals were precipitated with 10 mL of ethanol, collected after centrifugation, and redispersed in 10 mL of cyclohexane.

2.3 Synthesis of $CaGdF_5$ and CaF_2 precursor

To obtain 0.1 mmol per mL $CaGdF_5$ precursor for shell coating, 1 mmol CaO, 0.5 mmol Gd_2O_3, and 5 mmol trifluoroacetic acid were added to a 100 mL flask and heated to 50 °C under vigorous stirring. After the system became a clear solution, 5 mL of oleic acid and 5 mL of 1-octadecene were added, and the solution was heated to 100 °C for 10 min and then to 156 °C for 30 min. The precursor is finally cooled to room temperature and waiting to use. The CaF_2 precursor is obtained by the same method using only CaO instead of CaO and Gd_2O_3.

2.4 Synthesis of core@shell $CaGdF_5$:20% Yb,2% Er@CaGdF_5 NPs (CGF@CGF) and $CaGdF_5$:20% Yb,2% Er@CaF_2 NPs (CGF@CF)

To obtain core@shell NPs, a solution of 0.2 mmol core $CaGdF_5$:Yb,Er nanocrystals in 2 mL of cyclohexane was added to the solution of 5 mL of oleic acid and 5 mL of 1-octadecene. Then the solution was kept at 70 °C for 30 min. After the cyclohexane was evaporated, the solution was heated to 300 °C under an argon atmosphere. The shell precursor is injected with a 0.02 mL min^{-1} rate into the solution. The core@shell nanocrystals were precipitated with 10 mL of ethanol, collected after centrifugation, and redispersed in 10 mL of cyclohexane.

3 Results and discussion

In order to acquire uniform and monodispersed CaLnF host-based UCNPs, the thermal decomposition method was explored. To ensure the successful formation of CaLnF NPs, a set of UCNPs samples (cores) (S1–3) were synthesized by changing the molar ratio of Ca to Gd acetate salts from 0:1 to 2:1. Transmission electron microscope (TEM) images in Fig. 1a–c show monodisperse and small diameters of 4.5 ± 1.2 nm, 4.6 ± 1.0 nm, and 4.0 ± 1.1 nm for S1, S2, and S3, respectively (Fig. 1d and S1†). From X-ray diffraction (XRD) patterns, the peaks of S1 well agreed with the characteristic peaks of orthorhombic GdF_3, and the peaks became broadband due to their relatively small size. As we can see, the morphology of GdF_3 NPs is oval, and coincide with their orthorhombic phase. Those XRD peaks of S2 and S3 well agreed with the characteristic peaks of cubic $Ca_{0.55}Gd_{0.3}F_2$, indicating the synthetic $Ca_xGd_yF_{(2x+3y)}$ samples are $Ca_{0.55}Gd_{0.3}F_2$ crystals (denoted as CaGdF). The alkaline-earth rare-earth fluoride (MLnF) host is based on the MF_2 crystal structure and every alkaline-earth cation position can be exchanged with rare-earth cations.[27] To ensure all the Gd^{3+} ions were doped in the CaGdF NPs, the Ca^{2+}/Gd^{3+} ratio was increased from 1:1 to 2:1. Compared to the GdF_3 NPs, the spherical NPs of CaGdF are observed in Fig. 1b and c. The size of S3 is slightly smaller than
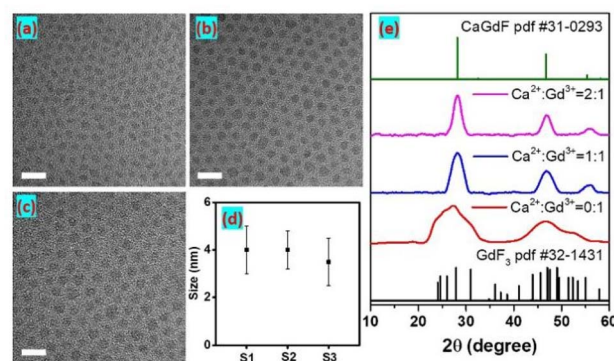

Fig. 1 TEM images of (a) S1, (b) S2, and (c) S3 $Ca_xGd_yF_{(2x+3y)}$ samples with the molar ratio of Ca^{2+} to Gd^{3+} (0:1, 1:1, and 2:1, respectively), scale bar: 5 nm; (d) the size and (e) XRD patterns of three $Ca_xGd_yF_{(2x+3y)}$ samples.

that of S2, since the extra Ca^{2+} ions would produce more nuclear and decrease the average particle volume. Fig. S2† shows the energy dispersive spectrometer (EDS) patterns of the CaGdF NPs with Ca^{2+}/Gd^{3+} molar ratio of 1 : 1, which reveals that the synthesized products are composed of F, Ca, Gd, Yb and Er.

Next, the UCL performance of as-obtained UCNPs was studied under 980 nm excitation, as seen in Fig. 2a. The Yb^{3+} as sensitizers strongly absorb the excitation irradiation and transfer the excited energy to the nearby Er^{3+} emitter to produce upconversion emissions.

The CaGdF:Yb/Er (20/2 mol%) NPs exhibited characteristic emission peaks resulting from $^2H_{11/2}$, $^4S_{3/2} \rightarrow {}^4I_{15/2}$ (520–550 nm), and $^4F_{9/2} \rightarrow {}^4I_{15/2}$ (640–670 nm) transitions of Er^{3+}. Fig. S3† displays the UC integrated intensity bar chart of the samples with fixed Yb/Er (20%/2%) and varying Ca^{2+}/Gd^{3+} molar ratio. The UC emission intensity drastically increased with the increase of Ca^{2+}/Gd^{3+} from 0 : 1 to 1 : 1 due to the added Ca^{3+} ions changing the symmetry of the crystal lattice from orthorhombic GdF_3 to cubic CaGdF, and increasing the transition possibility of emitter ions. That is to say, the CaGdF host matrix is better than GdF_3 for upconversion emissions. When the Ca^{2+}/Gd^{3+} molar ratio increased to 2 : 1, the UC emission kept almost the same intensity, indicating that CaGdF:Yb,Er were successfully synthesized with a Ca^{2+}/Gd^{3+} molar ratio of more than 1 : 1, which is consistent with the XRD results. Compared to CaF_2:20% Yb,2% Er NPs, CaGdF:20% Yb,2% Er showed stronger UCL (Fig. S4†), which suggested that the added Gd^{3+} reduced the symmetry of the CaF_2 crystal lattice and increased the transition possibility of Er^{3+} ions. As we can see, CaGdF:20% Yb,2% Er NPs showed stronger luminescence intensity than $NaGdF_4$:20% Yb,2% Er with similar size, which is consistent with the previous work.[29] This may be related to the fact that the value of cation doping concentration in CaGdF is closer to the set optimal value. In general, the smaller the particle size, the lower the UCL efficiency because more quenching defects are generated on their surface as size decreases (specific surface area increases). Therefore, an optically inert shell is needed to prevent the excited state energy from coupling to the surface defects and thus quench the UCL. Next, we studied the UCL performance of homogeneous shells (CGF@CGF) and heteroepitaxial shells (CGF@CF). For comparison, the same core and same moles of injection precursor were employed during the

shelling procedure. The TEM and high resolution TEM (HR-TEM) images of core@shell UCNPs are shown in Fig. 3a and b, presenting a diameter of 8.2 ± 0.2 nm for CGF@CGF nanospheres and an edge length of 7.0 ± 0.1 nm for CGF@CF nanocubes. It can be found a typical core–shell structure of CGF@CF NPs because the lanthanide ions (Gd^{3+}) show high contrast (darker) over Ca^{2+}. However, the core–shell structure of CGF@CGF NPs failed due to the same composition in the core and shell layers. Furthermore, to study the shell growth kinetics of these two structures, we took intermediate samples at different precursor injection time points.

As we can see from TEM images (Fig. S5†), morphological change of CGF@CF NPs from spherical to cubic is observed after the second aliquot when the nanoparticle size exceeds approximately 6 nm. For CGF@CGF NPs, however, remain nearly spherical. This morphology could be related to a kinetically dominated shell growth regime due to the larger lattice parameters of CaGdF-based host. Furthermore, XRD analysis revealed the detailed lattice changes caused by different interfacial strains and epitaxial shell growth (Fig. 3c). It can be found that the diffraction peaks of CGF@CGF shift toward lower angles for Gd^{3+} doping in the host lattice because of the larger lattice parameters according to the Bragg diffraction equation.

Then, we investigated the UCL intensities of these two core@shell samples. To ensure that the UCL intensities of the two kinds of NPs were comparable, we calculated the effective diameter by equating the cubic volume with the spherical volume. For example, the CGF@CF sample with an edge length of 7.0 ± 0.1 nm converts into an effective diameter of 8.1 nm, comparable to spherical CGF@CGF particles. As we can see, upon 980 nm excitation, the upconversion emission was greatly enhanced by coating the NPs with both CaGdF and CaF_2 shells. Interestingly, the CGF@CF NPs with CaF_2 shell are more efficient in upconversion than those with CaGdF shell and the green to red ratio in CGF@CGF NPs is smaller than CGF@CF NPs (Fig. 3d). The luminescence intensity of energy level of lanthanide ions is expressed as below:
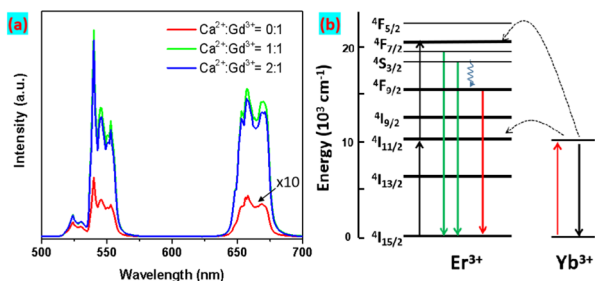

Fig. 2 (a) Upconversion emission spectra of the $Ca_xGd_yF_{(2x+3y)}$ samples under 980 nm excitation (10 W cm^{-2}). (b) Simplified energy level diagrams of Er^{3+} and Yb^{3+} ions and proposed energy-transfer mechanisms under 980 nm excitation.
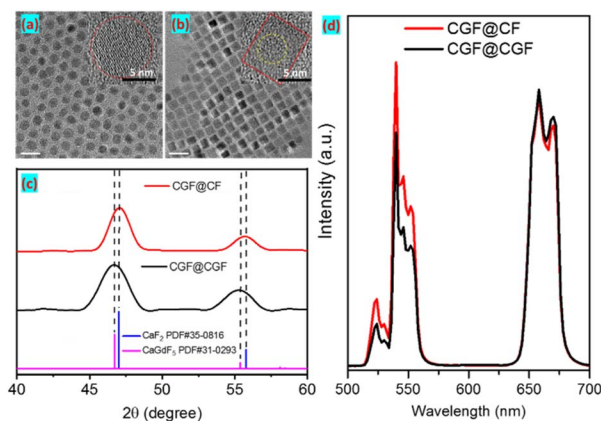

Fig. 3 TEM images of (a) CGF@CGF and (b) CGF@CF NPs, scale bar: 20 nm. Inset: HR-TEM of CGF@CGF and CGF@CF, scale bar 5 nm. (c) XRD patterns of CGF@CGF and (b) CGF@CF NPs. (d) Upconversion emission spectra of the core@shell UCNP samples at 10 W cm^{-2}.

$$I = \frac{I_0 A_r}{A_r + W_{nr}} \qquad (1)$$

where, I_0 is a constant, A_r is the radiative transition rate, W_{nr} is the multiphonon nonradiative relaxation rate. For UCL of CGF@CGF and CGF@CF NPs, the values of A_r are the same because the luminescent Er^{3+} ions are in the same host lattice and the same core. Therefore, the stronger UC emission of the latter is due to the smaller nonradiative relaxation rate W_{nr}, which is showed in Fig. 2b.

We next investigated the performance of the CGF@shell NPs as a temperature sensor in the 200–300 K range. The emission intensity ratio of the 520 nm ($^2H_{11/2} \rightarrow {}^4I_{15/2}$) to the 540 nm ($^4S_{3/2} \rightarrow {}^4I_{15/2}$) shows a strong temperature dependence because the $^2H_{11/2}$ and $^4S_{3/2}$ states of Er^{3+} ions are thermally coupled. It is observed that the emission band at 520 nm increases with the increasing temperature from 200 to 300 K after being normalized at the peak of 540 nm (Fig. 4a and b). Only several hundred wavenumbers separate these two states, and the thermal equilibrium of states population is determined by the Boltzmann distribution.

In our study, the thermometric parameter LIR is defined as the intensity ratio of the two emission peaks, which shows an excellent exponential relationship, described as follows:

$$\text{LIR} = \frac{I_{520}}{I_{540}} = C \times \exp\left(-\frac{\Delta E}{k_B T}\right) \qquad (2)$$

where C is a constant, T is the absolute temperature, ΔE is the energy gap between excited states of $^2H_{11/2}$ and $^4S_{3/2}$, and k_B is the Boltzmann constant. From eqn (2), we can see that the LIR is independent of photons since the theoretical model only considers the Boltzmann distribution and radiative transitions between two thermally coupled levels ($^2H_{11/2}$ and $^4S_{3/2}$). However, the nonradiative relaxation could not be neglected in the upconversion processes at high temperatures due to the

increased multiphonon relaxation. From the fitting of ln(LIR) *vs.* $1/T$ in Fig. 4c, the linear behavior is obtained with the slope values of −512 and −928 for CGF@CGF and CGF@CF UCNPs, respectively. It indicates that the temperature increase has a stronger influence on the UCL of CGF@CF than that of CGF@CGF. This consequent can be supported by the lifetime of upconversion emission in Fig. S6.† As we can see, the lifetime of upconversion emission at 520 nm or 540 nm for CGF@CGF only changed slightly while the lifetime for CGF@CF changed a lot when the temperature increased from 200 K to 300 K. Thus, the CGF@CF nanocrystals provide a luminescent probe for radiometric thermometry. The XRD pattern (Fig. 3c) revealed that the crystal plane spacing of the CaF_2 lattice was smaller than that of CaGdF with the same crystal plane index, which was in agreement with their difference in lattice constants (CaF_2: $a = 5.46$ Å, CaGdF: $a = 5.50$ Å). Besides, after coating with a CaF_2 shell, the peaks of CGF@CF NPs had a lightly right shift compared to those of CGF@CGF NPs. It means that there is noticeable lattice distortion at the interface of $CaGdF@CaF_2$. That means the interface lattice distortion can benefit the process of sensing temperature. A similar result has been reported in $NaGdF_4@$-$NaYF_4$ heterojunctions.[30]

Based on the ratiometric thermometer parameter, the relative sensitivity (S_r) was calculated by eqn (3):

$$S_r = \frac{1}{\text{LIR}}\frac{\partial \text{LIR}}{\partial T} = \frac{\Delta E}{k_B T} \qquad (3)$$

The dependence of relative thermal sensitivity S_r on temperature is shown in Fig. 4d, revealing that the maximum relative thermal sensitivity reaches an ultrahigh value of 2.20% K^{-1} at 200 K for CGF@CF NPs, which is higher than the value of 1.28% K^{-1} for CGF@CGF. Additionally, the relative thermal sensitivity of CGF@CF UCNPs (200 K) is more promising than that of similar reported UCNPs, as shown in Table S1.† Based on the results outlined, the excellent performance of the CGF@CF as a sensitive luminescence thermometer makes them promising candidates for applications where the temperature needs to be monitored with high precision and real-time. In Fig. S7,† we demonstrate the potential of this luminescent temperature probe for an *in situ* measurement technique in an extreme environment, such as a space satellite. Under the excitation of 980 nm diode lasers, a spectrometer collects the luminescence spectra, and the corresponding temperature changes can be obtained in real-time.
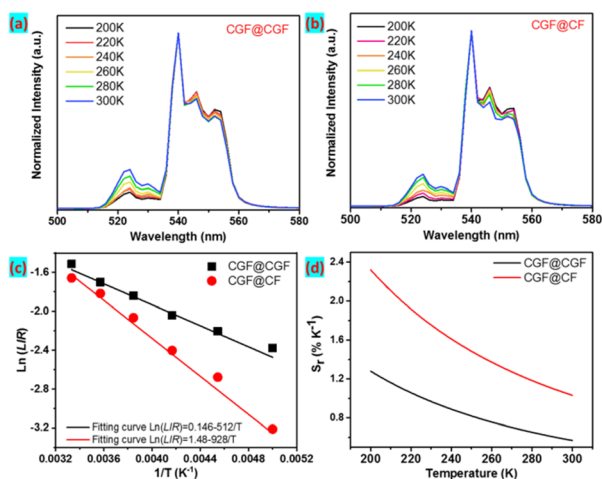

Fig. 4 Normalized emission spectra of (a) CGF@CGF and (b) CGF@CF. core@shell NPs as a function of temperature under 980 nm excitation. (c) LIR of 520 nm and 540 nm as a function of temperature. (d) Relative thermal sensitivity of the CGF@CGF (black curve) and CGF@CF (red curve) NPs in the temperature range of 200–300 K.

4 Conclusions

We have developed a coprecipitation synthesis method to synthesize ultra-small and efficient lanthanide-doped core@-shell UCNPs. By optimizing of Ca^{2+}/Gd^{3+} molar ratio, sub-5 nm alkaline-earth rare-earth fluoride cores were prepared. On the one hand, Gd^{3+} ions doping can reduce the CaF_2 lattice symmetry, enhancing UCL. On the other hand, compared with homogeneous CaGdF shell of CGF@CGF NPs, heterogeneous CaF_2 shell of CGF@CF NPs further increases the UCL intensity. Notably, the CGF@CF heterostructure is more sensitive to

temperature changes due to lattice distortion in the interface, which is particularly interesting as multiphoton nanoprobes for applications in temperature sensing.

Author contributions

Y. C. and Q. L. conceived the experiments. X. X., H. C., W. W., and performed the experiments. X. X., Q. L., B. L., X. K., and Y. C. analyzed the data and prepared the manuscript. All authors contributed to manuscript writing and discussions.

Conflicts of interest

There are no conflicts to declare.

Acknowledgements

Notes and references

1 D. Baziulyte-Paulaviciene, N. Traskina, R. Vargalis, A. Katelnikovas and S. Sakirzanovas, *J. Lumin.*, 2019, **215**, 116672–116679.

2 D. Li, Q. Shao, Y. Dong and J. Jiang, *J. Alloys Compd.*, 2014, **617**, 1–6.

3 C. Hu, L. Lei, E. Liu, Z. Lu and S. Xu, *J. Lumin.*, 2022, **247**, 118905–118910.

4 S. W. Hao, G. Y. Chen and C. H. Yang, *Theranostics*, 2013, **3**, 331–345.

5 X. F. Wang, Q. Liu, Y. Y. Bu, C. S. Liu, T. Liu and X. H. Yan, *RSC Adv.*, 2015, **5**, 86219–86236.

6 G. G. Lin and D. Y. Jin, *ACS Sens.*, 2021, **6**, 4272–4282.

7 A. Nexha, J. J. Carvajal, M. C. Pujol, F. Diaz and M. Aguilo, *Nanoscale*, 2021, **13**, 7913–7987.

8 H. Liu, X. K. Jian, M. T. Liu, K. L. Wang, G. Y. Bai and Y. H. Zhang, *RSC Adv.*, 2021, **11**, 36689–36697.

9 Y. F. Bai, Y. Yang, Y. W. Deng, S. H. Dang, Z. L. He, Z. W. Zhou and L. Liu, *J. Phys. Chem. C*, 2022, **126**, 3830–3838.

10 W. Li, D. Wang, X. F. Li, P. Li, P. Fu, C. C. Hu, J. G. Hao, W. Li and Q. W. Zhang, *J. Mater. Chem. C*, 2022, **10**, 11891–11902.

11 J. S. Liao, M. H. Wang, F. L. Lin, Z. Han, B. A. Fu, D. T. Tu, X. Y. Chen, B. Qiu and H. R. Wen, *Nat. Commun.*, 2022, **13**, 2090–2100.

12 H. Liu, H. Y. Wang, X. K. Zheng, P. C. Wang and Y. H. Zhang, *Dalton Trans.*, 2022, **51**, 13106–13118.

13 M. Y. Luo, X. Z. Sha, B. J. Chen, X. Z. Zhang, H. Q. Yu, X. P. Li, J. S. Zhang, S. Xu, Y. Z. Cao, Y. C. Wang, X. Wang, Y. H. Zhang, D. Gao and L. Wang, *J. Am. Ceram. Soc.*, 2022, **105**, 3353–3363.

14 S. Y. Han, R. R. Deng, X. J. Xie and X. G. Liu, *Angew. Chem., Int. Ed.*, 2014, **53**, 11702–11715.

15 B. Golesorkhi, H. Nozary, A. Furstenberg and C. Piguet, *Mater. Horiz.*, 2020, **7**, 1279–1296.

16 B. Ren, B. Chen, J. Zhao, Y. Guo, X. Zhang, X. Chen, Y. Du, Z. Deng, G. Zhu and F. Wang, *Chem. Mater.*, 2020, **33**, 158–163.

17 F. Wang and X. G. Liu, *Chem. Soc. Rev.*, 2009, **38**, 976–989.

18 F. Wang, D. Banerjee, Y. S. Liu, X. Y. Chen and X. G. Liu, *Analyst*, 2010, **135**, 1839–1854.

19 S. Fischer, C. Siefe, D. F. Swearer, C. A. McLellan, A. P. Alivisatos and J. A. Dionne, *Angew. Chem., Int. Ed. Engl.*, 2020, **59**, 21603–21612.

20 F. Vetrone, V. Mahalingam and J. A. Capobianco, *Chem. Mater.*, 2009, **21**, 1847–1851.

21 M. Zeng, S. Singh, Z. Hens, J. Liu, F. Artizzu and R. Van Deun, *J. Mater. Chem. C*, 2019, **7**, 2014–2021.

22 Z. C. Li, D. C. Zhou, L. R. Jensen, J. B. Qiu, Y. F. Zhang and Y. Z. Yue, *J. Am. Ceram. Soc.*, 2021, **104**, 4471–4478.

23 F. Y. Ren, Y. Li, E. Y. B. Pun and H. Lin, *J. Phys. Chem. C*, 2021, **125**, 12107–12117.

24 S. Chen, Z. Chu, L. Cao, L. Xu, Q. Jin, N. Liu, B. Chen, M. Fang, W. Wang, H. Qian and M. Shao, *Nano Res.*, 2022, **15**, 9298–9308.

25 Z. Chu, T. Tian, Z. Tao, J. Yang, B. Chen, H. Chen, W. Wang, P. Yin, X. Xia, H. Wang and H. Qian, *Bioact. Mater.*, 2022, **17**, 71–80.

26 K. Liu, X. Yan, Y.-J. Xu, L. Dong, L.-N. Hao, Y.-H. Song, F. Li, Y. Su, Y.-D. Wu, H.-S. Qian, W. Tao, X.-Z. Yang, W. Zhou and Y. Lu, *Biomater. Sci.*, 2017, **5**, 2403–2415.

27 S. Fischer, R. D. Mehlenbacher, A. Lay, C. Siefe, A. P. Alivisatos and J. A. Dionne, *Nano Lett.*, 2019, **19**, 3878–3885.

28 X. Wu, S. Zhan, J. Han and Y. Liu, *Nano Lett.*, 2021, **21**, 272–278.

29 S. Fischer, R. D. Mehlenbacher, A. Lay, C. Siefe, A. P. Alivisatos and J. A. Dionne, *Nano Lett.*, 2019, **19**, 3878–3885.

30 X. Wu, S. Zhan, J. Han and Y. Liu, *Nano Lett.*, 2021, **21**, 272–278.